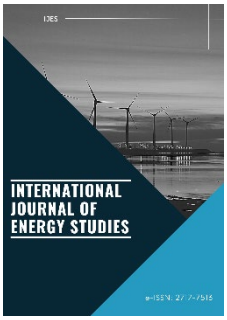
INTERNATIONAL JOURNAL OF ENERGY STUDIES

e-ISSN: 2717-7513 (ONLINE); homepage: https://dergipark.org.tr/en/pub/ijes



Research Article
Int J Energy Studies 2026; 11(2): 1165-1189
DOI: 10.58559/ijes.1929835

Received : 14 Apr 2026
Revised : 01 May 2026
Accepted : 18 May 2026

Investigation of electromagnetic energy propagation and shielding effectiveness in additively manufactured custom unit cells: A parametric study of geometry-dependent effects

Nail Kaya [a*], Ömer Keleş [b]

[a]*Gazi University, Graduate School of Natural and Applied Sciences, Department of Mechanical Engineering, Ankara, Turkey, ORCID : 0009-0000-8588-683X*

[b]*Gazi University, Faculty of Engineering, Department of Mechanical Engineering, Ankara, Turkey, ORCID : 0000-0002-3480-3456*

*(*Corresponding Author: 198310407@gazi.edu.tr)*

Highlights

- Investigating geometry-dependent electromagnetic energy propagation and shielding effectiveness in custom unit cells.
- Increasing shielding effectiveness through extended electromagnetic wave propagation paths.
- Achieving high SE through tortuosity and surface area optimization in lightweight structures.
- Proposing geometry-driven design guidelines for shielding optimization
- Demonstrating tunable electromagnetic shielding by SLM-fabricated AlSi10Mg custom unit cells.

You can cite this article as: Kaya N, Keleş Ö. Investigation of electromagnetic energy propagation and shielding effectiveness in additively manufactured custom unit cells: A parametric study of geometry-dependent effects. Int J Energy Studies 2026; 11(2): 1165-1189

ABSTRACT

Controlling electromagnetic energy propagation through geometric design has become a critical parameter for optimizing shielding performance in modern engineering applications. In this paper, geometry-dependent electromagnetic energy propagation and shielding effectiveness in additively manufactured custom unit cells are systematically investigated. The unit cells were classified into three main geometric groups, each consisting of four channel profile variants with controlled geometric modifications, and their SE performance was characterized through combined numerical simulations and experimental measurements over the 1–12 GHz frequency range. The unit cell configurations were analyzed based on geometric parameters, including internal surface area, tortuosity factor, and weight reduction. The results indicate that surface area and tortuosity are strongly correlated with shielding effectiveness, whereas weight reduction shows a limited contribution to shielding performance. By controlling these parameters, electromagnetic energy propagation within the structure can be effectively manipulated, providing a powerful design strategy to optimize shielding performance beyond conventional aperture-based approaches.

Keywords: Additive manufacturing, Electromagnetic energy, Custom unit cell, Shielding effectiveness

1. INTRODUCTION

Electromagnetic (EM) energy is generated by natural sources and various electronic systems, including electrical-electronic and electromechanical devices. Natural sources consist of events such as solar flares, lightning, and cosmic radiation, whereas electronic systems such as high-frequency circuits, motors, power systems, and radars act as artificial sources of EM energy. These sources can cause EM interference, which may disrupt signal integrity in electronic systems, potentially leading to data loss, system malfunctions, or even security vulnerabilities. One of the most effective methods for preventing EM interference is EM shielding, which uses a barrier to reduce the transmission of EM energy through reflection, absorption, and multiple internal reflections [1-3].

Shielding materials are designed as continuous and aperture-free structures to minimize EM energy leakage. However, engineering design constraints require apertures for cable routing, ventilation, thermal management, weight reduction, control panel integration, and maintenance access [4-7]. The presence of apertures in shielding materials alters wave–structure interaction mechanisms, including multiple internal reflections, scattering, and extended propagation paths, thereby influencing the EM shielding behavior. Therefore, geometrical features such as aperture shape, size, continuity, and distribution are primary design parameters in determining the overall SE [8-11]. Controlling these parameters enables the manipulation of wave propagation within the structure, offering an effective approach to increase shielding performance beyond conventional material-based design strategies. The investigation of aperture effects on SE has therefore attracted extensive research efforts through analytical, numerical, and experimental approaches [12-18].

Basyigit et al. [19] investigated the effects of aperture size and polarization type on the electrical SE of metallic enclosures by comparing experimental measurements with CST-EMC simulations based on the finite integration technique over the frequency range of 2.6–9 GHz. Three enclosures with dimensions of 160 mm x 160 mm x 800 mm were tested, each featuring apertures of different aspect ratios but identical total aperture area (75 x 75 mm, 150 x 37.5 mm, and 300 x 18.75 mm). Both vertical and horizontal positioning of the transmitting antenna with respect to the longitudinal aperture orientation were investigated. The results demonstrated that rectangular apertures consistently provided higher SE than square apertures, with improvements ranging between 5 dB to 28 dB. Vertical antenna positioning resulted in increased shielding performance compared to horizontal positioning, with shielding capabilities exceeding 65%, 70%, and 77% for the 75 × 75

mm, 150 × 37.5 mm, and 300 × 18.75 mm apertures, respectively. Araneo et al. [20] analyzed the influence of aperture wall thickness on SE using a second-order method of moments formulation with mixed-potential integral equations. Simulation results showed that increasing wall thickness provided a consistent overall SE improvement, although the increment was limited to approximately 2–3 dB below 3 GHz for practical thicknesses. Hu et al. [21] proposed a hybrid model combining a circuit model and full-wave method for estimating the SE of empty metallic enclosures with ventilation apertures of arbitrary shape or aperture arrays of arbitrary distribution on one side. The perforated enclosure was split into a perforated plate and a semi-enclosed rectangular waveguide shorted at the end. The S parameters of the perforated plate were calculated using the CST Microwave Studio software. Khorrami et al. [22] developed a multiresolution method of moments approach for efficiently calculating the shielding effectiveness of metallic enclosures with arbitrarily shaped apertures. The proposed method produced sparse impedance matrices, reduced computational cost, and provided results in good agreement with experimental measurements. The study also demonstrated that aperture shape, arrangement, and spacing significantly influence the shielding performance of metallic enclosures. Dehkhoda et al. [23] developed a technique to evaluate the SE of a rectangular enclosure of finite wall thickness and with numerous square or circular small apertures, subject to a normally incident plane wave. The technique was based on the traditional waveguide circuit model, where the enclosure is replaced with an equivalent shorted transmission line. The main innovation was that in the proposed circuit model, the perforated thick wall is represented by an equivalent impedance derived from the reflection coefficient, rather than the coplanar strip transmission line used in Robinson's original model. The Robinson model is not accurately predict the effect of aperture thickness on SE, particularly at larger thicknesses. Guo et al. [24] analytically modeled the SE of single-layer perforated cavities. Results showed that circular aperture arrays exhibited better shielding performance than rectangular ones, with the circular configuration achieving approximately 14 dB higher SE at 0.5 GHz. An internal dielectric plate considerably increased SE near the resonance frequency, while the resonant frequency gradually decreased from the reference value of 0.7 GHz as the dielectric plate thickness increased. Kumar and Venkatesh [25] performed an analysis of the SE of rectangular and cylindrical enclosures with rectangular and circular apertures using transmission line matrix modeling method. This study provided insights into how both the enclosure geometry and the aperture shape influence the shielding performance. The method was employed to simulate the SE of different enclosure-aperture combinations, enabling a systematic comparison across multiple geometrical configurations. He et al. [26] investigated the shielding

performance of a metallic enclosure with slots using both numerical modeling and experimental measurements. Based on their results, they developed the modeling approach and provided practical insights into the design of shielded enclosures with slots for cable penetration and ventilation purposes. Kwon et al. (27) proposed a composite absorber structure incorporating both dielectric and magnetic absorbers within a dual- metal-panel enclosure to prevent EM leakage due to apertures. The study analyzed a 0.6 × 0.5 × 0.8 m metallic enclosure with 100 × 10 mm apertures over the 1 MHz – 3 GHz frequency range using CST MWS. The composite absorber demonstrated a minimum reduction effect of approximately 50 dB across the entire frequency range. They reported increasing the distance between apertures on the inner and outer panels significantly improved SE, while absorber thickness had a minimal impact on overall shielding performance. Rabat et al. [28] analyzed the SE of different aperture geometries using the intermediate level circuit model. The aim was to develop a fast and accurate analytical model for circular, elliptical, round-ended, and cross-shaped apertures. The model was applied for four different aperture geometries on an enclosure measuring 30×12×26 cm ($\sigma = 10^5$ S/m), and results were compared with full-wave numerical methods. Approximately 10 dB SE difference was observed between circular and elliptical apertures of the same area. The model computation time was under 2 seconds, providing significant advantage over the hours-long computation times of full-wave methods.

Studies in the literature demonstrate that, beyond material properties, parameters such as aperture geometry, orientation, polarization relationship, and wall thickness strongly influence SE. This shows that geometric design of shielding materials can be considered a critical engineering parameter in controlling EM energy propagation. Although aperture-based EM shielding has been extensively studied, most studies focus on simple geometries such as rectangular and circular apertures, as well as canonical periodic structures. However, understanding how controlled geometric variation of internal pathways affects electromagnetic wave propagation mechanisms and SE remains inadequately characterized over a wide frequency range. The ability to fabricate complex internal geometries that cannot be produced using conventional manufacturing methods through advancing additive manufacturing technologies is expected to further increase the importance of research in this field. To reveal the effect of controlled geometric variations in internal surfaces on SE, this study investigates custom unit cells fabricated via selective laser melting (SLM).

2. MATERIALS AND METHODS

2.1. Modeling of custom unit cell

Geometric configurations of the custom unit cells were parametrically modeled by varying the tortuosity factor (Figure 1). Tortuosity factor (L_{eff}/L_{geo}) is defined as the ratio of actual path length to geometric path (straight-line distance) through the unit cell [29-31].

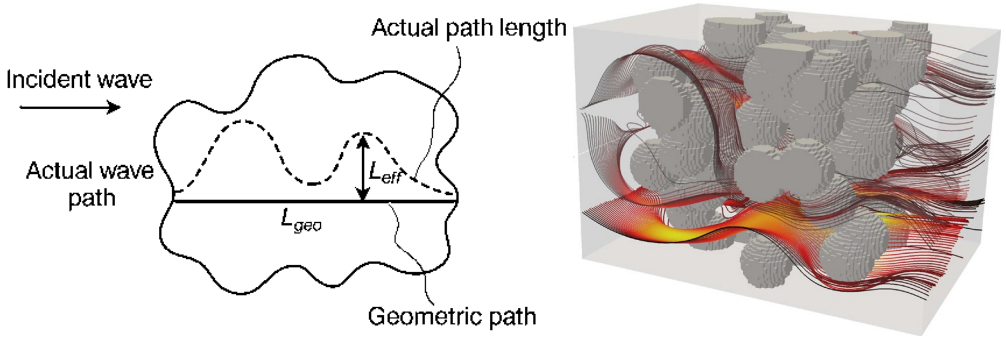


Figure 1. Schematic illustration of the tortuosity (wave path elongation factor) [31]

Three tortuosity groups (A1, A2, A3) defined the baseline complexity of the internal paths, while four path profile variants within each group systematically varied the cross-sectional geometry. This resulted in a total of twelve distinct custom unit cell configurations designed to investigate the effects of geometric variations on SE. All custom unit cells have identical external dimensions of 21 mm × 21 mm × 5 mm. The geometric details and classification of the unite cells are shown in Figure 2 and Figure 3, respectively.

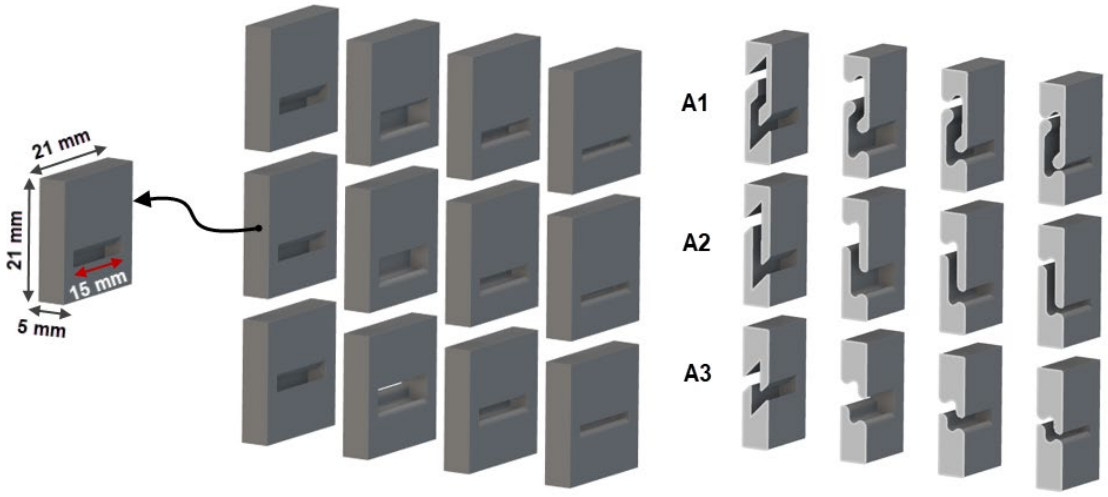


Figure 2. Geometric details of custom unite cells a) Unit cell size b) Unite cell configurations c) Section of unit cell

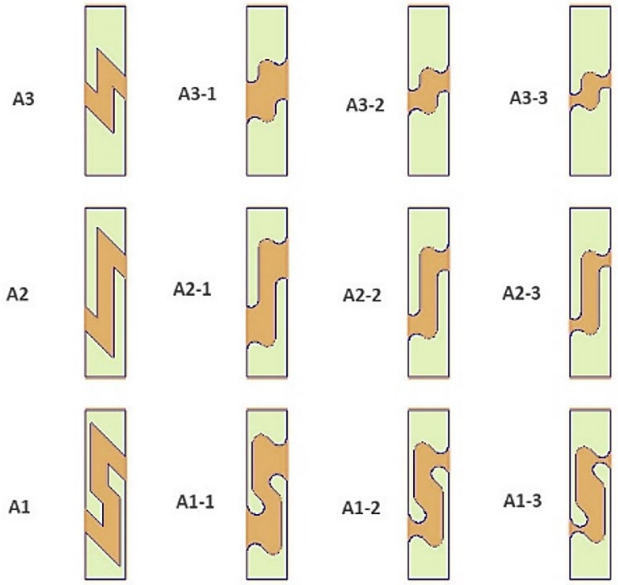


Figure 3. Classification and labeling of the custom unit cell configurations and their corresponding path profile variants

Geometric properties of the unit cells, including volume, surface area, tortuosity factor, and weight reduction, were determined through MATLAB-based computational analysis of STL mesh data. The results are summarized in Table 1. The mass of the reference solid specimen (without internal channels) was assumed to be 5.90 g, based on an AlSi10Mg density of 2.67 g/cm³. This value was used in weight reduction calculations.

Table 1. Geometric propetries of the unit cell configurations

Unit Cell	Volume (mm³)	Mass (g)	Tortuosity factor	Surface Area (mm²)	Weight Reduction (%)
A1	1527.6	4.08	5.14	1972.7	30.8
A1-1	1489.0	3.98	5.61	1759.3	32.6
A1-2	1637.2	4.37	4.56	1799.4	25.9
A1-3	1712.4	4.57	4.55	1819.5	22.5
A2	1653.9	4.42	4.24	1829.0	25.1
A2-1	1623.2	4.33	3.07	1620.6	26.5
A2-2	1749.0	4.67	3.29	1660.7	20.8
A2-3	1829.8	4.89	2.67	1680.8	17.1
A3	1829.2	4.88	3.27	1637.6	17.2
A3-1	1799.5	4.80	2.96	1428.6	18.5
A3-2	1944.3	5.19	2.19	1468.7	11.9
A3-3	2035.0	5.43	1.66	1488.8	7.8

The geometric details of the specimen A2 is shown in Figure 4. The remaining specimen configurations were designed using the same principles and dimensions. Specimens A1, A2, and A3 are illustrated as representative examples in Fig. 5, respectively.

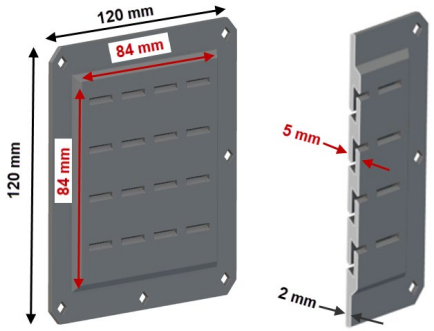


Figure 4. Geometric details of the specimen A2

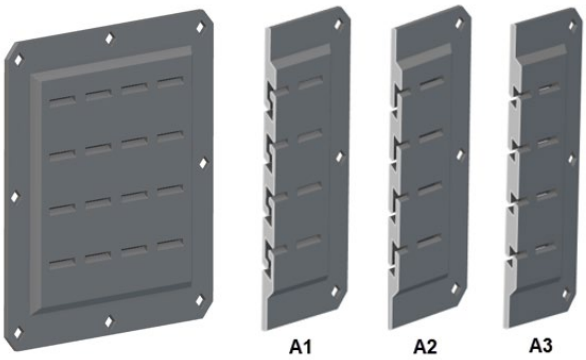


Figure 5. Geometric configurations of specimens A1, A2, and A3

The specimens were modeled as periodic lattice structures using the custom unit cells in the nTop platform, based on an equation-driven implicit modeling approach. nTop defines geometries through mathematical equations and supports the efficient parametric control of unit-cell topologies and geometric parameters, allowing the rapid generation of complex lattice geometries. Geometric parameters such as minimum feature size, curvature radius, and pathway continuity were carefully selected to ensure that the designed unit cells could be fabricated without requiring additional support structures. This support-free design reduces post-processing requirements and prevents residual powder that can adversely affect EM wave propagation.

2.2. Numerical analyses setup

Full-wave EM simulations were conducted using ANSYS HFSS to analyze the SE of the unit cell configurations. Floquet port excitation with master–slave periodic boundary conditions was

applied to a single unit-cell domain to model the EM response of an infinite periodic array. Two Floquet ports were positioned at a distance of λ/2 above and below the unit cell surfaces, while the de-embedding planes coincided with the unit cell boundaries. The λ/2 distance was selected to minimize near-field effects and ensure that the incident wave approximated a uniform plane wave before interacting with the structure. This distance reduced the influence of evanescent fields while maintaining computational efficiency. The wavelength was taken as the maximum value within the 1–12 GHz frequency range (λ = 300 mm at 1 GHz).

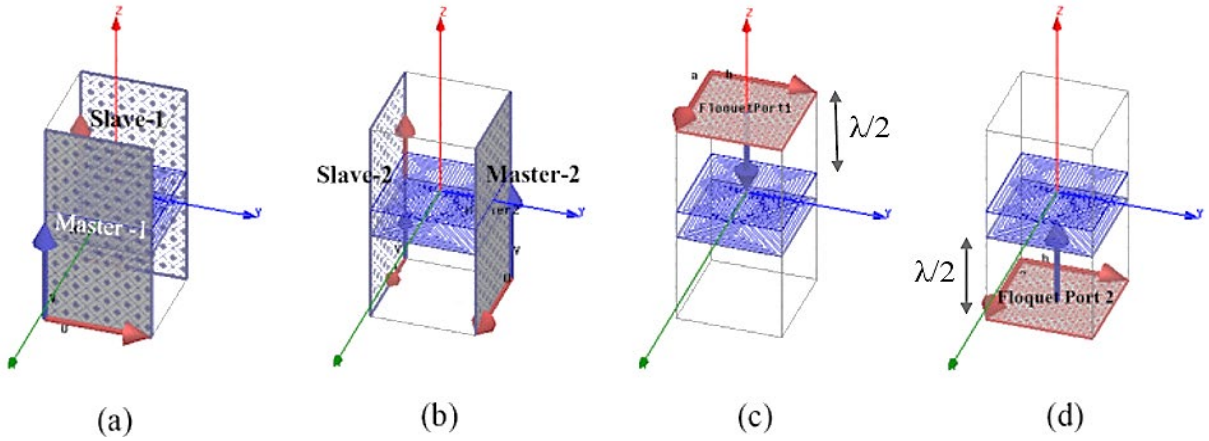


Figure 6. a) and b) Master-slave boundary condition, c) Floquet port 1 and d) Floquet port 2 [32]

Adaptive mesh refinement with a convergence criterion of $\Delta S < 0.02$ was employed. Interpolating sweep was used for frequency sweep analysis. The simulations were performed over the 1–12 GHz frequency range using an interpolating sweep with a frequency step size of 1 GHz. The material properties of SLM-processed AlSi10Mg vary depending on the printing parameters and post-processing heat treatment conditions. A T6 heat treatment was applied to the test specimens after SLM fabrication. In the simulations, the electrical conductivity of the T6 heat-treated specimens was defined as 2.7×10^7 S/m [33]. Due to the symmetry of the unit cells, only the S21 parameter was used in the calculation of SE, as shown in Figure 7.

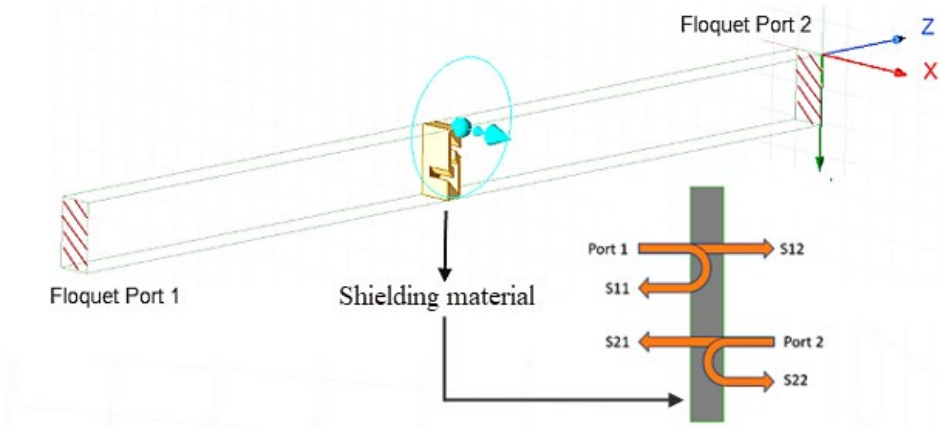


Figure 7. S-parameters of shielding material

As shown in Figure 8, EM wave wave can be incident on the unit cell surface at various elevation (θ) and azimuthal (φ) angles. In this study, the analysis was performed only under normal incidence conditions (θ = 0°, φ = 0°). Under these conditions, the EM wave propagates perpendicular to the unit cell boundaries, while the polarization is determined by the orientation of the electric field within the transverse plane.

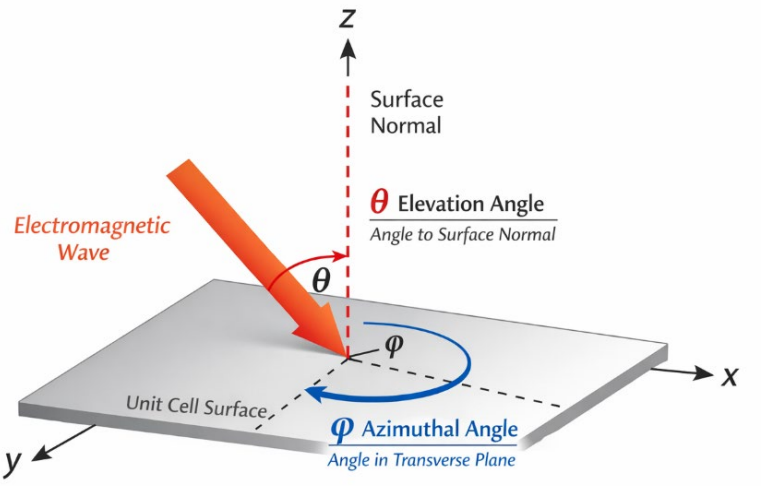


Figure 8. Schematic illustration of elevation (θ) and azimuthal (φ) angles

When the aperture length is parallel to the electric field direction, EM leakage increases, resulting in a significant reduction in SE. To ensure measurable data within the dynamic range of the measurement system, excitation was applied along the longer dimension of the aperture, as shown in Figure 9 (a).

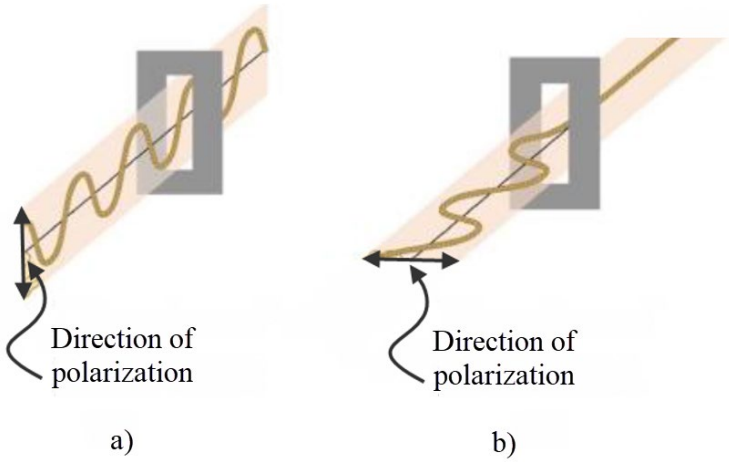


Figure 9. a) and b) Schematic illustration of electric field polarization directions

2.3. Additive manufacturing of test specimens

Additive manufacturing (AM) enables the fabrication of unit cell geometries with complex internal channels that are not feasible using conventional manufacturing methods. In this study, custom-designed unit cell configurations were fabricated from AlSi10Mg aluminum alloy via selective laser melting (SLM).

The specimens were fabricated using a Concept Laser M2 system wiht gas-atomized AlSi10Mg powder supplied by Advanced Powders and Coating. The powder has a spherical morphology with a particle size distribution ranging from 10 to 63 μm. All samples were fabricated with a layer thickness of 40 μm to preserve intricate lattice features, particularly the micrometer-scale wall thickness. The manufacturing process was carried out under a nitrogen atmosphere with a pre-heated build platform at 150 °C. Dual Yb-fiber lasers were employed with a scan speed of 1300 mm/s and a hatch spacing of 150 μm. A bidirectional continuous scanning strategy combined with a 67° inter-layer rotation was applied to minimize anisotropic residual stresses and increase geometric accuracy. The laser spot size during scanning was 115 μm. For surface contouring, a separate parameter set was employed with dual 200 W laser power, a scan speed of 700 mm/s, and a reduced laser spot size of 75 μm to improve surface quality and dimensional precision.

The STL files were converted into production files using Materialise Magics software. Prior to manufacturing, integrity checks were performed on the exported STL data in Magics to eliminate topological inconsistencies, which could result in defects during laser scanning. The specimens were oriented vertically on the build plate to reduce thermal stress and maintain dimensional

stability. The layouts relative to each other and the laser starting point were tailored to a uniform cooling regime. All samples were sliced to a 40 μm layer thickness to preserve intricate lattice features, particularly the micrometer-scale wall thickness.

The extraction of unmelted metal powders from the intricate internal channels of the SLM-produced specimens is critical. Residual powders within the structure can increase the specimen weight and cause deviations in EM measurements by altering the effective pore size and geometric characteristics of the lattice. After the test specimens were removed from the build plate, a four-step post-processing procedure was employed, including compressed air cleaning, ultrasonic cleaning in ethanol, and drying. Ultrasonic cleaning was performed for 3 min for each specimen. This cleaning process (Figure 10) ensured that the physical samples closely matched the ideal geometry of the numerical models and minimized its impact on SE.



Figure 10. a) Test specimens during the removal process from the SLM system, b) Compressed air cleaning, and c) Ultrasonic cleaning process

2.4. Experimental setup

The EM shielding performance of the SLM-fabricated AlSi10Mg specimens was experimentally assessed using a measurement setup configured in accordance with IEEE Std 299-2006. Schematic diagram of the experimental setup is illustrated in Figure 11. A receiving antenna (ETS 3117) was positioned inside the anechoic chamber and connected to a signal analyzer (Rohde & Schwarz FSV) located outside the chamber. A transmitting antenna (ETS 3115), driven by a signal generator (Rohde & Schwarz SMF), was also placed outside the chamber (Figure 12).

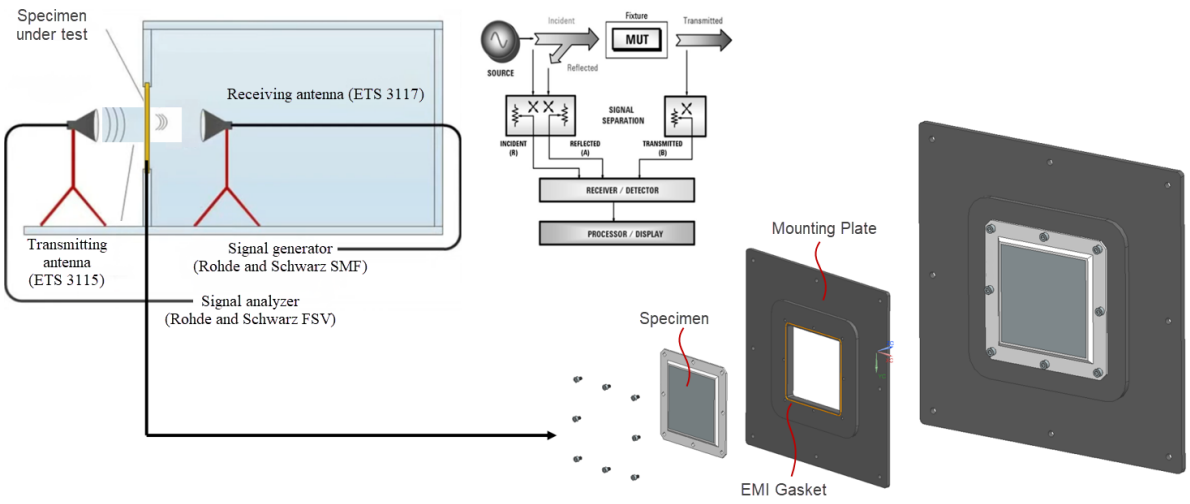
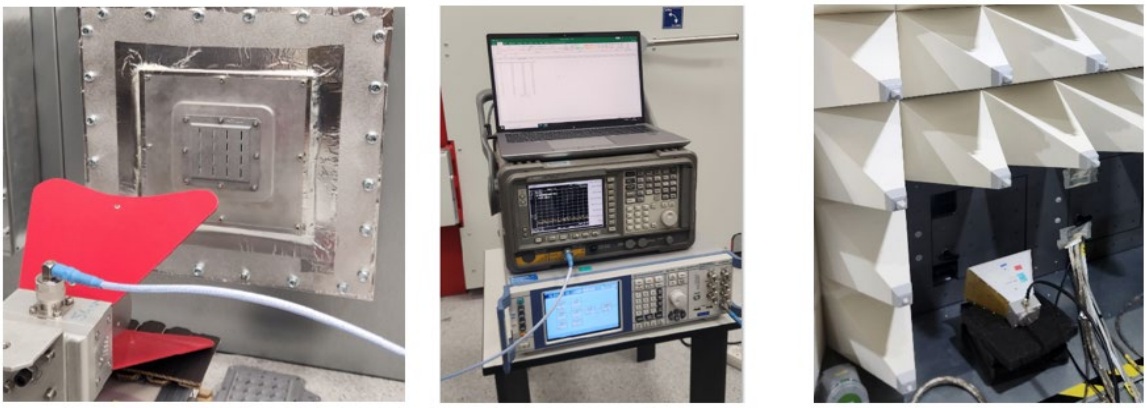


Figure 11. Schematic diagram of the experimental setup for shielding SE measurements

The transmitting antenna was positioned in the source chamber at a distance of 1 m from the aperture window, while the receiving antenna was placed at the same distance on the opposite side. In order to determine the SE, two measurements were conducted as reference and loaded cases. The reference measurements were performed using only the mounting plate, without any specimen, to characterize the baseline EM transmission of the experimental setup. In the loaded measurement, the test signal was transmitted through the specimen placed on the mounting plate. The SE was calculated as the difference between the reference and loaded transmission levels. The mounting plate was fabricated from the same material as the specimens, and its electrical conductivity was assumed to be identical to that of the specimens ($\sigma = 2.7 \times 10^7$ S/m). All loaded measurements were obtained using the same mounting plate; thus, its influence on the SE remained consistent across all specimens and had negligible impact on the comparative results. To prevent EM leakage, an EMI gasket (CHO-SEAL 1285) was used between the specimen and the mounting plate, ensuring reliable electrical contact and repeatable measurements.



a) b) c)

Figure 12. (a) Exterior view of the anechoic chamber, (b) Signal analyzer and signal generator, and, (c) Interior view of the anechoic chamber.

3. RESULTS AND ANALYSIS

3.1. Shielding effectiveness results of the specimens

The numerical and experimental SE results demonstrate similar frequency-dependent behavior across the investigated 1–12 GHz range. The numerical results of specimens A3-3 and A1-3 from three-dimensional ANSYS HFSS simulations are shown in Figure 13 and Figure 14, respectively. The remaining results are presented in graphical form in Figures 15–19.

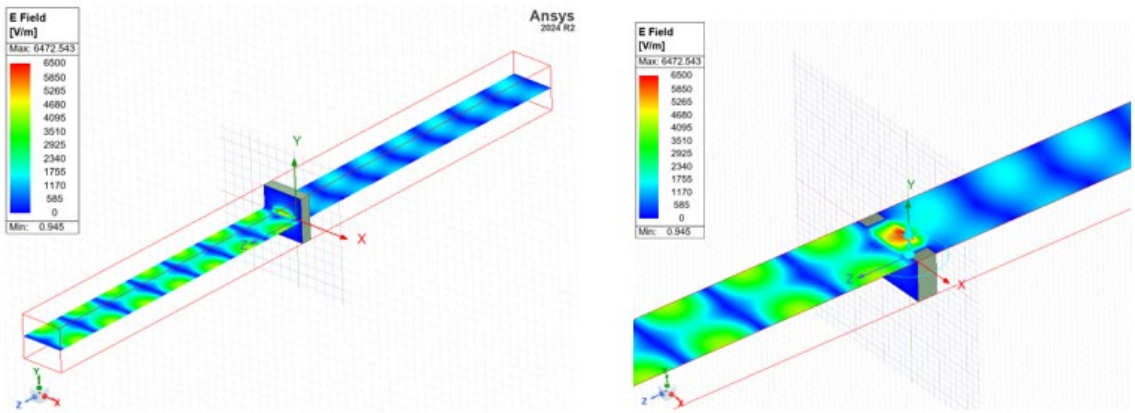


Figure 13. Numerical results of specimen A3-3 @10 GHz

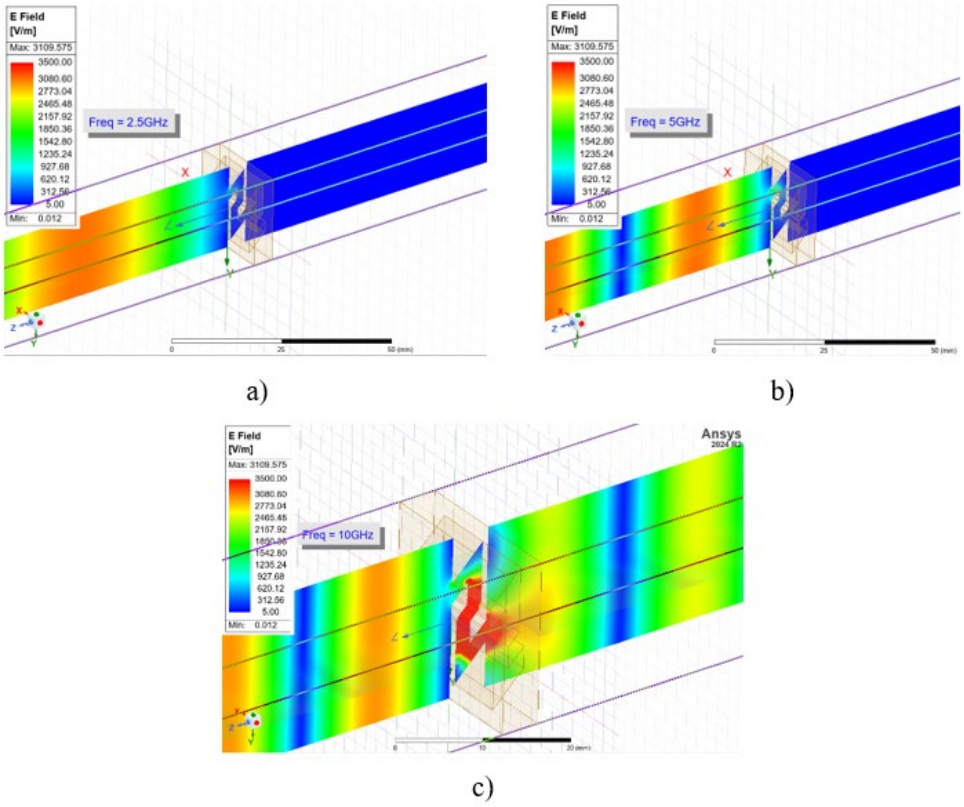


Figure 14. Numerical results of specimen A1 a) @ 2.5 GHz, b) @5 GHz, and c) @ 10 GHz

The three-dimensional ANSYS HFSS simulations illustrate the frequency- and geometry-dependent propagation of electromagnetic (EM) energy through the structure. At lower frequencies, the complex unit cell geometry increases the effective propagation path of the wave, promoting multiple reflections and energy dissipation, which improves shielding performance. As the frequency increases, however, the wavelength becomes comparable to the characteristic aperture dimensions, altering the primary wave–structure interaction mechanisms.

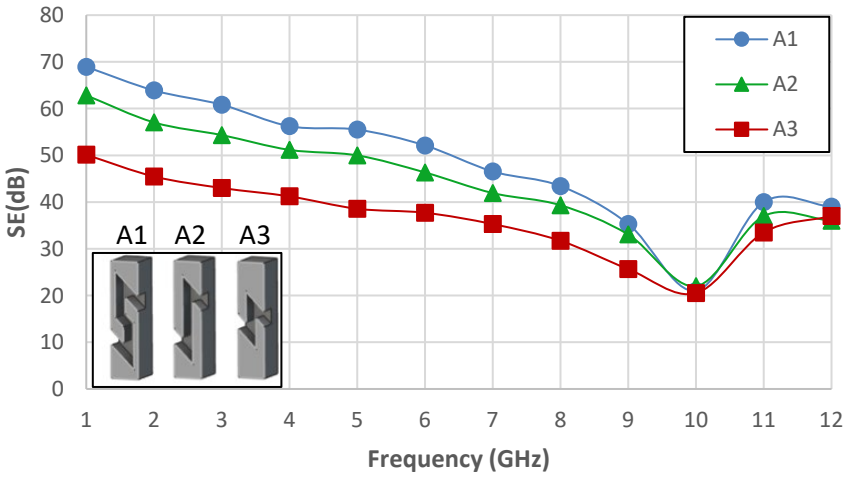


Figure 15. Numerical SE results of specimens A1, A2, and A3

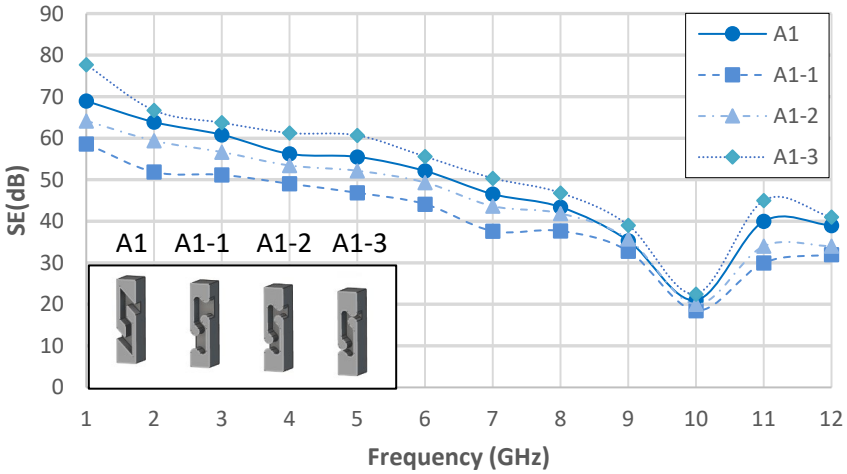


Figure 16. Numerical SE results of specimens A1, A1-1, A1-2, and A1-3

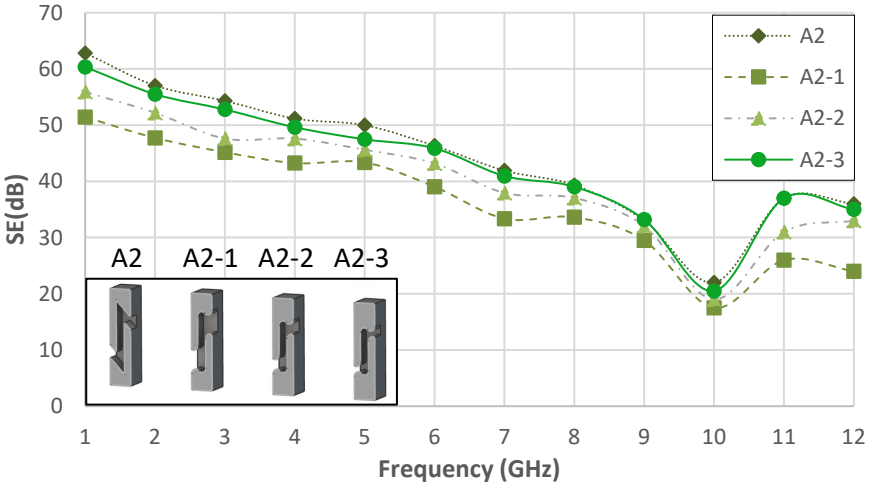


Figure 17. Numerical SE results of specimens A2, A2-1, A2-2, and A2-3

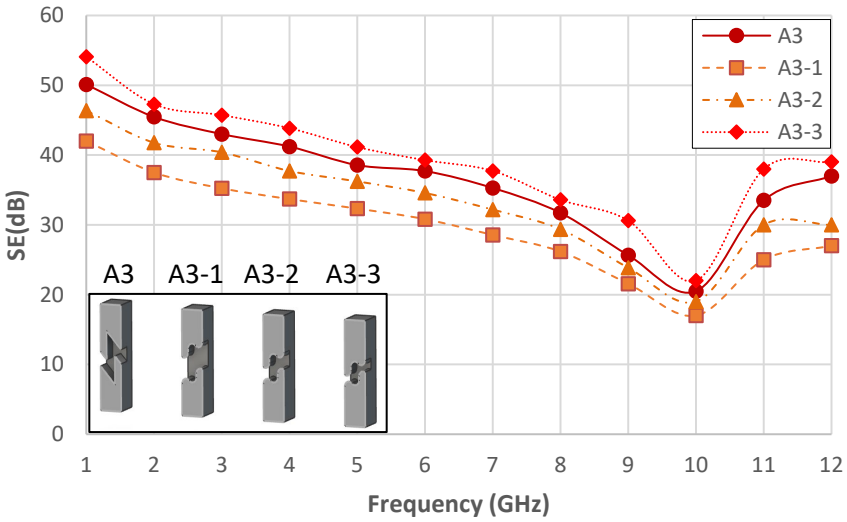


Figure 18. Numerical SE results of specimens A3, A3-1, A3-2, and A3-3

The results of the specimens achieving the highest and lowest SE are shown in Figure 19.

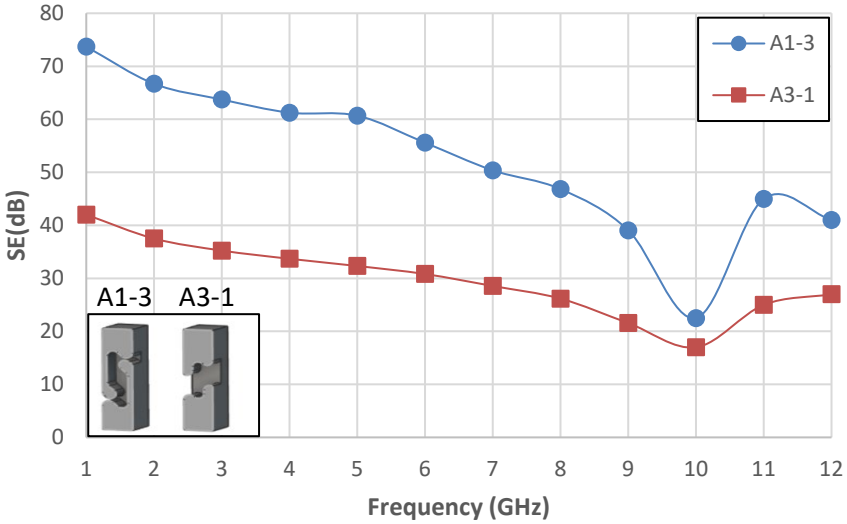


Figure 19. Numerical SE results of specimen A1-3 and A3-1

The results demonstrate that, by altering the EM wave propagation path within the unit cell, higher SE values can be achieved. For this configuration, an improvement of approximately 40 dB was achieved at low frequencies. An increase of 40 dB in SE results in a reduction of the transmitted electric field strength (E_t) by a factor of 100, as can be expressed based on the SE equation:

$$SE(dB) = 20log_{10}\left(\frac{E_i}{E_t}\right) \quad (1)$$

The reduction observed around 10 GHz across all configurations can be attributed to the relationship between the EM wavelength and the aperture dimensions of the unit cell. When the aperture dimensions approach approximately half the wavelength, the aperture exhibits slot-antenna-like behavior, resulting in increased EM transmission and a corresponding reduction in SE. As shown in Figure 2, the 15 mm rectangular slot on the unit-cell surface corresponds to approximately half the wavelength at around 10 GHz ($\lambda \approx 30$ mm). Under this condition, resonance-like behavior occurs within the apertures, which leads to increased EM transmission through the structure (Figure 14).

3.2. Analysis of deviations between numerical and experimental results

Experimental SE results for all specimens are summarized in Table 2. All results show similar frequency-dependent trends across the 1–12 GHz frequency range. The deviation analysis indicates an average difference of approximately 1.8 dB at low frequencies and 4.6 dB at high frequencies.

Table 2. Experimental SE results for all specimens (dB)

Frequency (GHz)	A1				A2				A3			
	A1	A1-1	A1-2	A1-3	A2	A2-1	A2-2	A2-3	A3	A3-1	A3-2	A3-3
1	69.6	59.6	64.3	78.9	63.2	50.3	55.3	61.2	50.1	42.4	47.6	55.8
2	64.8	52.1	58.9	67.7	57.3	46.6	51.9	58.9	46.3	37.5	42.6	48.3
3	60.2	52.7	55.2	64.9	54.5	44.1	48.8	55.1	44.7	38.5	42.6	47.0
4	56.4	50.8	53.0	63.6	52.3	43.5	48.8	52.1	42.7	36.8	39.3	45.9
5	55.7	46.0	51.5	61.2	50.3	44.2	47.7	51.9	41.2	33.8	38.2	43.0
6	53.1	44.0	49.2	60.7	48.6	40.1	43.6	48.1	38.2	32.4	35.9	40.0
7	50.6	38.5	44.2	51.8	41.6	33.3	38.0	44.3	37.7	31.4	33.8	39.6
8	47.2	38.5	42.7	47.0	40.2	33.9	37.2	41.9	36.6	26.1	31.1	38.1
9	43.2	33.4	36.2	40.2	35.6	30.2	33.3	37.8	31.5	25.7	30.3	33.4
10	22.1	20.5	22.2	22.1	29.8	18.4	28.0	30.9	25.0	18.5	22.3	25.6
11	40.6	30.5	33.6	45.6	25.6	25.5	31.8	37.1	33.2	25.0	30.5	39.6
12	40.7	32.3	33.4	41.3	24.4	24.1	35.5	38.3	38.3	27.6	30.4	38.7

These results demonstrate that surface roughness and dimensional tolerances from the SLM manufacturing process become more significant at higher frequencies, where shorter wavelengths are more sensitive to surface irregularities. The deviations also result from differences in the geometric resolution of the STL models used in the numerical simulations and fabrication processes. In the simulations, a geometric tolerance of 0.1 mm was selected to balance numerical stability, computational efficiency, and solution accuracy, whereas a coarser tolerance of 0.3 mm

was adopted during fabrication due to file size and processing constraints in the SLM workflow. The difference in geometric resolution leads to slight deviations in the fabricated structures, primarily resulting in enlarged aperture dimensions. Enlarged apertures increase the effective open cross-sectional area and reduce electromagnetic energy dissipation along the propagation path, thereby enabling greater transmission of incident waves through the unit cell. Consequently, the reduced geometric resolution of the fabricated specimens resulted in lower SE values across all investigated frequency bands. However, the magnitude of this deviation remained limited and had negligible impact on the comparison of SE trends among the custom unit cell configurations.

3.3. Analysis of the effects of weight reduction, surface area, and tortuosity on shielding effectiveness (SE)

Regression analysis was performed to examine the relationship between SE and the weight reduction, surface area, and tortuosity of the unit cells. To evaluate these relationships, two statistical metrics were applied in the regression analysis; the correlation coefficient (R) and the p-value. The correlation coefficient (R) measures the strength and direction of the linear relationship between the variables, whereas the p-value assesses the statistical significance of the relationship by estimating the probability that the observed correlation has occurred by chance. A high absolute value of R indicates a strong linear relationship, while a low p-value (typically $p < 0.05$) suggests that the relationship is statistically significant and not due to random variation [34].

The regression results demonstrated that weight reduction exhibits a low correlation with SE ($R = 0.344$, Figure 20), whereas SE shows a stronger correlation with the unit-cell surface area (Figure 21), with a frequency-averaged correlation coefficient of $R = 0.818$ across the 1–12 GHz frequency range. The data points closely follow a linear trend, and all tortuosity groups (A1–A3) align along the same regression, indicating that increased surface area facilitates stronger wave–material interaction, resulting in increased reflection and absorption losses. Geometrical variations that increase internal surface area within periodic structures provide a more effective design approach for optimizing EM shielding performance than methods based on increasing material density or overall material usage.

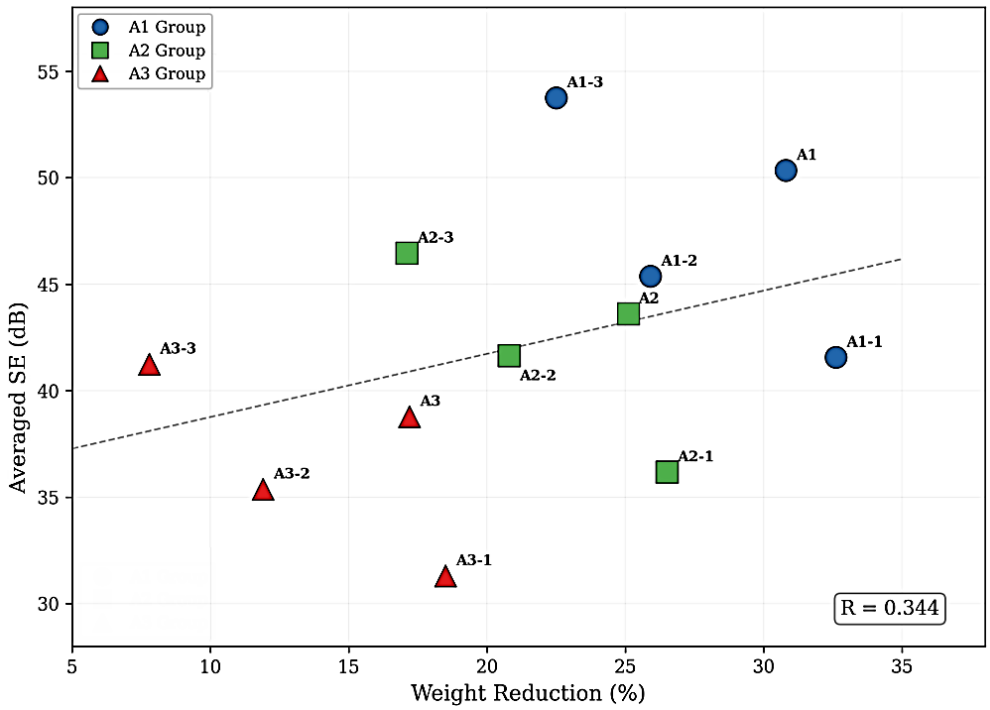


Figure 20. Regression analysis between weight reduction and averaged SE over the 1–12 GHz frequency band.

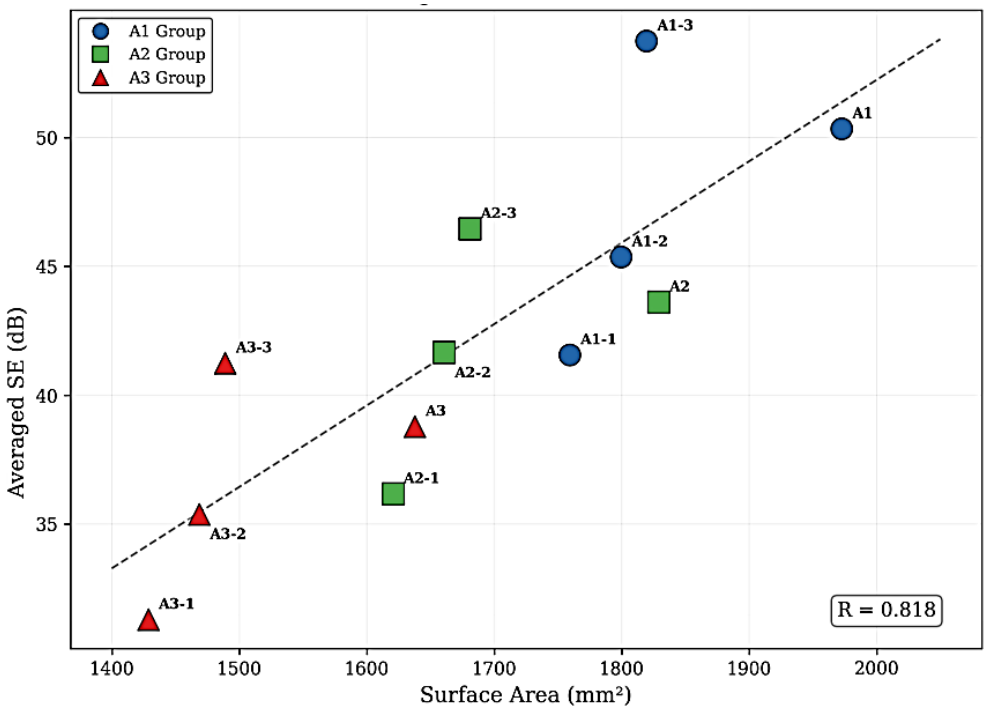


Figure 21. Regression analysis between surface area and averaged SE over the 1–12 GHz frequency band.

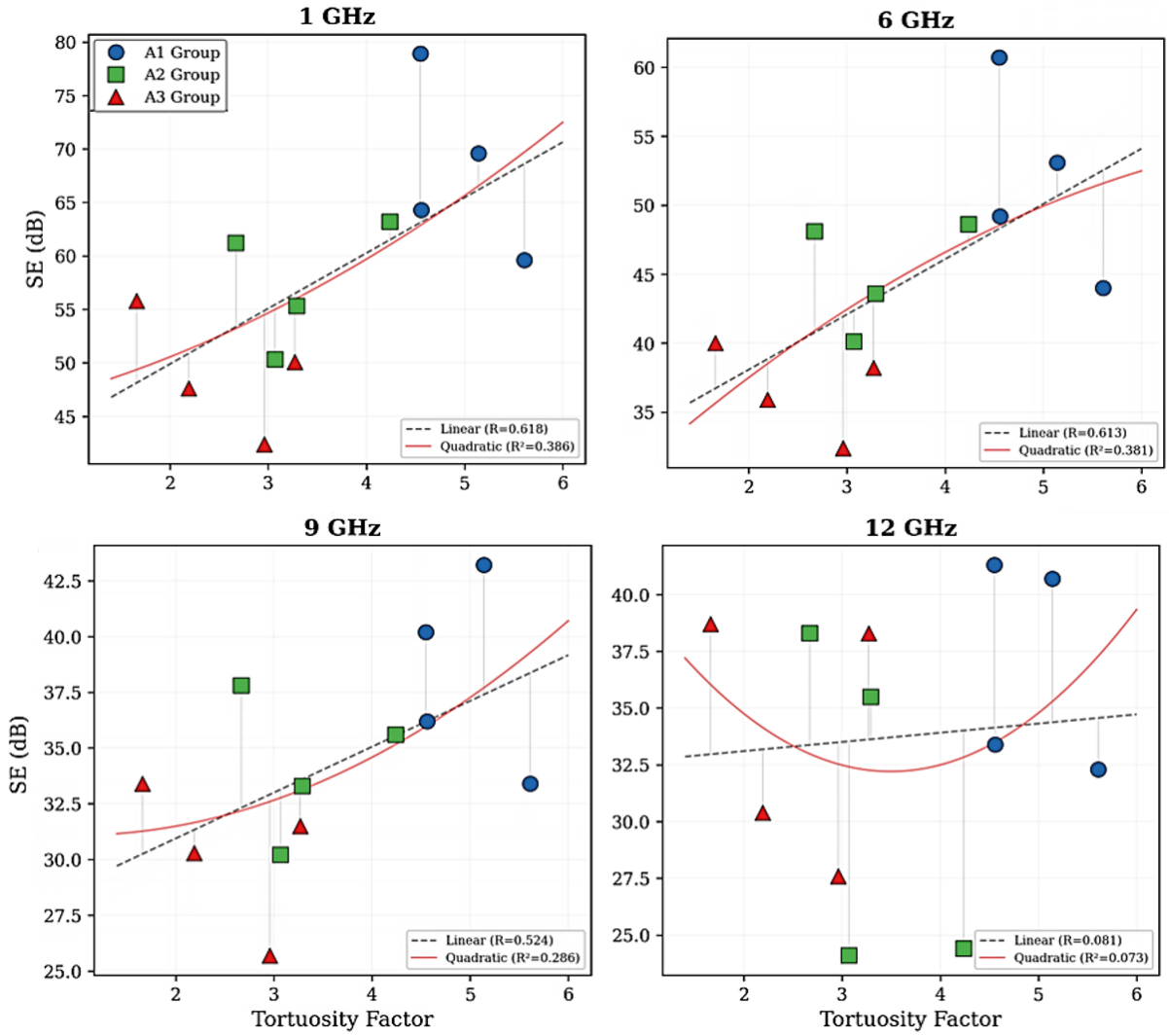


Figure 22. Regression analysis between tortuosity factor and averaged SE over the 1–12 GHz frequency band.

The tortuosity factor (τ) exhibits a limited correlation with SE in the low-to-mid frequency range (Figure 22). The correlation coefficient reaches R = 0.618 at 1 GHz and then gradually decreases with increasing frequency, approaching R ≈ 0.52 at 9 GHz. A clear group-wise separation is observed, where A1 (high τ) achieves the highest SE, A3 (low τ) the lowest, and A2 remains intermediate. This confirms that increased tortuosity leads to improved shielding performance.

3. CONCLUSION

In this study, the influence of parametrically designed custom unit cell configurations fabricated from AlSi10Mg alloy via selective laser melting on SE was systematically investigated. The unit cells were classified into three geometric groups with four channel profile variants each, and their SE performance was characterized through both numerical simulation and experimental

measurement across the 1–12 GHz frequency range. The variations in SE values clearly demonstrate that parametric unit cell design enables a broad and tunable EM shielding performance. The unit cell configurations were analyzed in terms of surface area, tortuosity factor, and weight reduction. The high correlation observed across the 1–12 GHz frequency range, with a frequency-averaged correlation coefficient of R = 0.818, indicates that surface area is the primary parameter influencing shielding performance. Between the groups with the highest and lowest tortuosity values (A1–A3), a 23% increase in surface area is associated with an improvement of 11.1 dB in averaged SE. At the configuration level, a 39% increase in surface area (from A3-1 to A1-3) results in a 26 dB increase in shielding performance. In contrast, weight reduction exhibits a relatively low correlation with SE (R = 0.344), indicating that material removal or addition alone is not improve shielding performance.

Based on the results, surface area and tortuosity directly influence the EM wave propagation path within the structure, increasing multiple internal reflections and associated absorption losses. These findings demonstrate a hierarchical relationship for EM shielding design optimization, in which surface area (R = 0.818) exhibits the strongest influence, followed by the tortuosity factor (R = 0.618 at 1 GHz), while weight reduction (R = 0.344) has the least effect. Accordingly, optimizing these parameters enables the development of lightweight structures with improved EM shielding performance. Furthermore, SLM enables the fabrication of geometrically complex shielding structures with highly tunable EM properties, offering strong potential for advanced engineering applications.

NOMENCLATURE

AM	Additively manufactured
CAD	Computer-aided design
EM	Electromagnetic
EMI	Electromagnetic Interferance
FDM	Fused deposition modeling
HFSS	High Frequency Structural Simulator
MWS	Microwave Studio
SE	Shielding effectiveness
SLM	Selective laser melting
STL	Stereolithography file format

ACKNOWLEDGMENT

We would like to thank ASELSAN Inc. for its support in the manufacturing and experimental processes.

DECLARATION OF ETHICAL STANDARDS

The authors of the paper submitted declare that nothing which is necessary for achieving the paper requires ethical committee and/or legal-special permissions.

CONTRIBUTION OF THE AUTHORS

Nail KAYA: Conceptualization, methodology, experimental investigation, formal analysis, data interpretation, writing-original draft, writing-review and editing.

Ömer KELEŞ: Supervision, conceptualization, methodology, validation, and writing-review and editing.

CONFLICT OF INTEREST

There is no conflict of interest in this study.

REFERENCES

[1] Tong XC. Advanced materials and design for electromagnetic ınterference shielding. CRC Press, 2009.

[2] Kihal MC, Azizi H, Chebout M, Sekki D, Kihal M, Moulai H. An improved circuit model for the estimation of the electromagnetic energy coupling throughout aperture into metallic enclosure. South Florida Journal of Development 2024; 5(11): 1-17.

[3] Paul CR. Introduction to electromagnetic compatibility. 2nd Ed. Wiley-Interscience, 2006.

[4] Yaslak HI. Assessment of shielding effectiveness by using electromagnetic topology method. MSc Thesis, Middle East Technical University, 2013.

[5] Devellioğlu Y. Electronic packaging and environmental test and analysis of an EMI shielded electronic unit for naval platform. MSc Thesis, Middle East Technical University, 2008.

[6] Parlak M. Thermal management with double layered heat sink produced by direct metal laser sintering. International Journal of Energy Studies 2024; 9(1): 155-173.

[7] Wang C, Wang Y, Zou F, Fang B, Zhao J, Zhang H, Guo J, Jia L, Yan D. Construction of lightweight, high-energy absorption 3D-printed scaffold for electromagnetic interference shielding with low reflection. Composites Part B 2025; 291: 112043.

[8] Olyslager F, Laermans E, De Zutter D, Criel S, De Smedt R, Lietaert N, De Clercq A. Numerical and experimental study of the shielding effectiveness of a metallic enclosure. IEEE Transactions on Electromagnetic Compatibility 1999; 41(3): 202-213.

[9] Basyigit IB, Dogan H, Helhel S. Simulation of metallic enclosures with apertures on electrical shielding effectiveness. International Conference on Electrical and Electronics Engineering (ELECO), Bursa, Turkey, 2017.

[10] Li M, Nuebel J, Drewniak JL, DuBroff RE, Hubing TH, Van Doren TP. EMI from airflow aperture arrays in shielding enclosures-experiments, FDTD, and MoM modeling. IEEE Transactions on Electromagnetic Compatibility 2000; 42(3): 265-275.

[11] Basyigit IB, Dogan H. The analytical and artificial intelligence methods to investigate the effects of aperture dimension ratio on electrical shielding effectiveness. International Journal of Electronics and Telecommunications 2019; 65(3): 359-365.

[12] Hu MZ, Wang Y, Liu Q, Wang N, Tang RK, Li XF. Analysis of factors influencing the shielding effectiveness of multi-layer cavity based on BLT equation. Chinese Astronomy and Astrophysics 2025; 49(2): 416-435.

[13] Shen S, Wang Y, Xing P. The prediction of shielding effectiveness of the rectangular enclosure with complex apertures based on the BLT equation. IEICE Electronics Express 2025; 21(1): 1-6.

[14] Hussain T, Cao Q, Majid I. Shielding effectiveness of enclosure with unconventional aperture array. Asia-Pacific Microwave Conference (APMC), Nanjing, China, 2015.

[15] Nouainia A, Hamdi B, Aguili T. Waveguide shielding analysis of 1D and 2D planar rectangular metallic structures using modified MoM-GEC method based on wave concept. Radiation Physics and Chemistry 2018; 150: 189-198.

[16] Azizi H, Chebout M, Moulai H, Bréard A, Vollaire C. Analytical and numerical models compared with measurements for analysis of electromagnetic radiation through apertures of a metallic enclosure. Serbian Journal of Electrical Engineering 2020; 17(2): 131-148.

[17] Ahmed I, Wan Mahadi WNL. Simulation of PCB enclosure with aperture for shielding 5G high frequency. IEEE International Conference on Artificial Intelligence in Engineering and Technology (IICAIET), Kuala Lumpur, Malaysia, 2022.

[18] Budnarowska M, Mizeracki J. Determination of shielding effectiveness of a subnanosecond high-power em ınterference by an enclosure with aperture using time domain approach. Energies 2023; 16(4): 1931.

[19] Basyigit IB, Genc A, Helhel S. Electrical shielding effectiveness of metallic enclosures; effect of source orientation and aperture dimension. Progress In Electromagnetics Research Symposium (PIERS), St Petersburg, Russia, 2017.

[20] Araneo R, Lovat G, Paulotto S. Effects of aperture thickness on the shielding effectiveness of metallic enclosures. IEEE International Symposium on Electromagnetic Compatibility, Honolulu, HI, USA, 2007.

[21] Hu PY, Sun XY, Chen J. Hybrid model for estimating the shielding effectiveness of metallic enclosures with arbitrary apertures. IET Science, Measurement & Technology 2020; 14(4): 462-470.

[22] Khorrami MA, Dehkhoda P, Mazanaran RM, Sadeghi SHH. Fast shielding effectiveness calculation of metallic enclosures with apertures using a multiresolution method of moments technique. IEEE Transactions on Electromagnetic Compatibility 2010; 52(1): 230-235.

[23] Dehkhoda P, Tavakoli A, Moini R. Fast calculation of the shielding effectiveness for a rectangular enclosure of finite wall thickness and with numerous small apertures. Progress In Electromagnetics Research 2008; 86: 341-355.

[24] Guo L, Shi X, Li X, Ma L, Guo C. Analysis of shielding effectiveness of a cavity with ınternal dielectric plate and apertures. Applied Sciences 2025; 15(5): 2460.

[25] Kumar TRS, Venkatesh C. Shielding effectiveness comparison of rectangular and cylindrical enclosures with rectangular and circular apertures using TLM modeling. Applied Electromagnetics Conference (AEMC), Kolkata, India 2009.

[26] He J, Schögenhofer P, Fyne K. Shielding performance of a metallic enclosure with slots - numerical modelling and measurements. International Symposium on Electromagnetic Compatibility, Beijing, China, 2002.

[27] Kwon JH, Hyoung CH, Park HH. Analysis of shielding performance in double-layered enclosures with ıntegrated absorbers. Electronics 2024; 13: 4345.

[28] Rabat A, Bonnet P, El Khamlichi Drissi K, Girard S. An analytical evaluation of the shielding effectiveness of enclosures containing complex apertures. IEEE Access 2021; 9: 147191-147204.

[29] Ghanbarian B, Hunt AG, Ewing RP, Sahimi M. Tortuosity in porous media: a critical review. Soil Science Society of America Journal 2013; 77: 1461-1477.

[30] Hamann T, Zhang L, Gong Y, Godbey G, Gritton J, McOwen D, Hitz G, Wachsman E. The effects of constriction factor and geometric tortuosity on Li-Ion transport in porous solid-state Li-Ion electrolytes. Advanced Functional Materials 2020; 30: 1910362.

[31] Matyka M, Koza Z. How to calculate tortuosity easily. AIP Conference Proceedings 2012; 1453:17-22

[32] Panchal S, Naresh Kumar M, Shreenidhi HS, Sahu PK, Abdullah MI, Malik J, Ravi Varma DVS, Singh U, Bhowmik A, Santhosh AJ. Dual-layer sub-6GHz 5G communication FSS with triple band-stop characteristics. Results in Engineering 2025; 27: 106495.

[33] Uliasz P, Knych T, Piwowarska M, Wiecheć J. The influence of heat treatment parameters on the electrical conductivity of AlSi7Mg and AlSi10Mg aluminum cast alloys. International Conference on Aluminum Alloys. Pittsburgh, US, 2016.

[34] Chatterjee S, Hadi AS. Regression analysis by example. John Wiley & Sons, Hoboken, US, 2012.